Chinese Chemical Letters 34 (2023) 108035

Contents lists available at ScienceDirect

Chinese Chemical Letters

journal homepage: www.elsevier.com/locate/cclet

Advances in component and operation optimization of solid oxide electrolysis cell

Xiaoxin Zhang[a], Bo Liu[b], Yanling Yang[a], Jianhui Li[d], Jian Li[b], Yingru Zhao[a], Lichao Jia[b,*], Yifei Sun[a,c,e,f,*]

[a] College of Energy, Xiamen University, Xiamen 361102, China
[b] School of Materials Science and Engineering, State Key Lab of Materials Processing and Die & Mould Technology, Huazhong University of Science and Technology, Wuhan 430074, China
[c] Innovation Laboratory for Sciences and Technologies of Energy Materials of Fujian Province (IKKEM), Xiamen 361005, China
[d] National Engineering Laboratory for Green Chemical Productions of Alcohols, Ethers and Esters, College of Chemistry and Chemical Engineering, Xiamen University, Xiamen 361005, China
[e] State Key Laboratory of Physical Chemistry of Solid Surfaces, College of Chemistry and Chemical Engineering, Xiamen University, Xiamen 361005, China
[f] Shenzhen Research Institute of Xiamen University, Shenzhen 518057, China

ARTICLE INFO

Article history:
Received 5 October 2022
Revised 23 October 2022
Accepted 29 November 2022
Available online 1 December 2022

Keywords:
Solid oxide electrolysis cell
Fuel assistant
Stack
Operation condition
Anode
Cathode

ABSTRACT

Considering the earth powered by intermittent renewable energy in the coming future, solid oxide electrolysis cell (SOEC) will play an indispensable role in efficient energy conversion and storage on demand. The thermolytic and kinetic merits grant SOEC a bright potential to be directly integrated with electrical grid and downstream chemical synthesis process. Meanwhile, the scientific community are still endeavoring to pursue the SOEC assembled with better materials and operated at a more energy-efficient way. In this review article, at cell level, we focus on the recent development of electrolyte, cathode, anode and buffer layer materials for both steam and CO_2 electrolysis. On the other hand, we also discuss the next generation SOEC operated with the assistant of other fuels to further reduce the energy consumption and enhance the productivity of the electrolyzer. And stack level, the sealant, interconnect and stack operation strategies are collectively covered. Finally, the challenges and future research direction in SOECs are included.

1. Introduction

The fast development of the global economy heavily relies on the exploration and utilization of fossil fuels such as crude oil and natural gas [1]. The excessive consumption of carbon-based energy carriers results in the raising level of CO_2 emission in atmosphere over 410 ppm in 2018, 40% higher than that before "industry revolution" [2]. The "biological carbon cycle" in nature with the participation of plants could only make limited contribution to the alleviation of this challenge *via* the natural photosynthesis, and severe environmental and ecological issues have been brought due to the CO_2 emission induced climate change [3]. Therefore, the revolution of our current energy system: *i.e.*, the technologies for artificial capture/conversion of CO_2 and promoted share of low/zero carbon energy (such as H_2) are urgently required [4]. With the consideration of low weight energy storage density and high cost of lithium battery (<260 Wh/kg, >100 USD/kWh) [5], an ideal renewable system calls for advanced resolutions transforming fluctuating renewable electricity (wind or solar) into clean, value-added and transportable chemicals/fuels for continuous demands and multipurpose. Recent studies have illustrated that approximately half of the renewable electricity system requires further reasonable energy storage section. And an estimated value could be over 7500 terawatt-hours in Euro to realize completely decarbonization [6]. Thereby, the high-efficient electrolysis is undoubtedly the core step toward the realization of 100% renewable earth, which essentially consumes "exhausted carbon" to produce "valuable carbon" or convert H_2O into H_2, completing the gap in carbon neutral cycle with near-zero emission [7].

So far, the electrolysis cells with different configurations and working principles are reported, including alkaline electrolysis cells (AECs), polymer electrolyte membrane electrolysis cells (PEMECs), and solid oxide electrolysis cells (SOECs). The AECs cell typically contains two electrodes isolated by a separator immersed in an aqueous alkaline solution (*e.g.*, KOH). But the corrosive liquid

* Corresponding authors.
E-mail addresses: jialc@hust.edu.cn (L. Jia), yfsun@xmu.edu.cn (Y. Sun).

https://doi.org/10.1016/j.cclet.2022.108035
1001-8417/

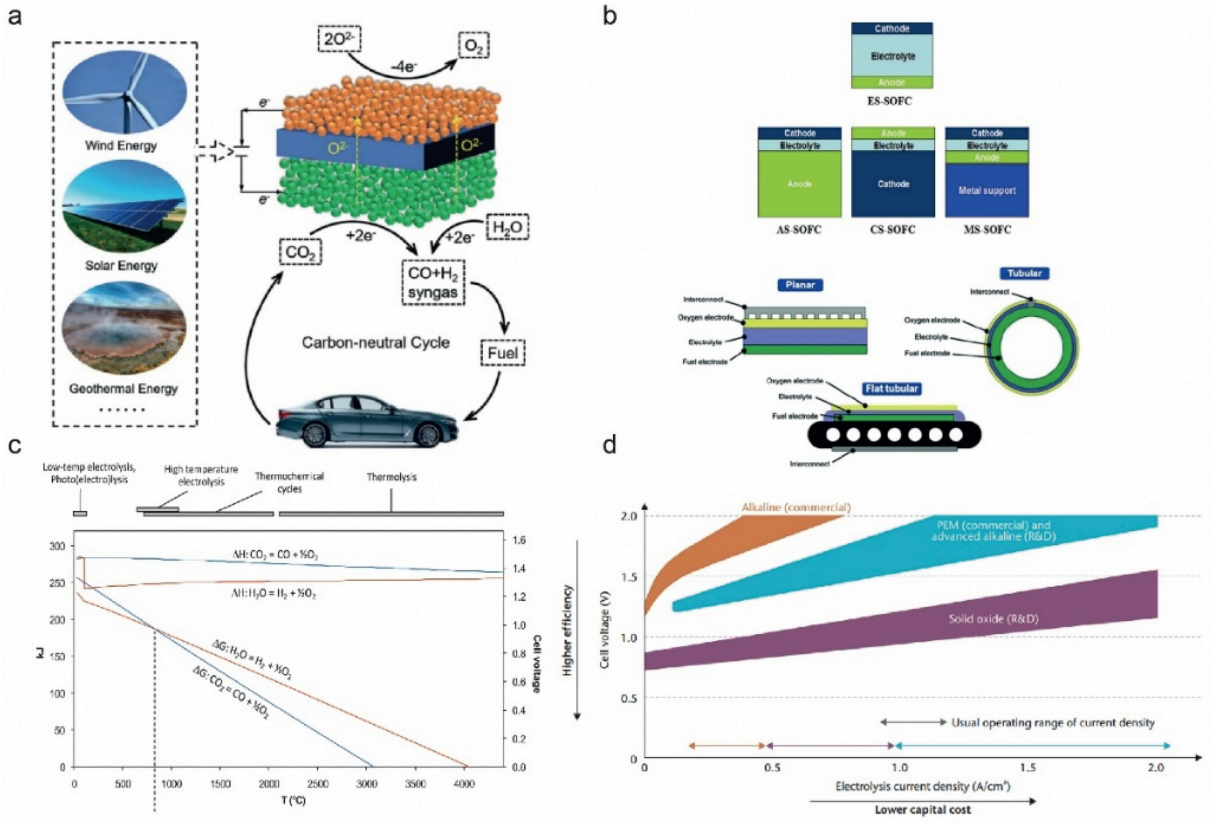

Fig. 1. (a) The schematic of carbon neutral cycle based on renewable energy and solid oxide electrolysis cell. Copied with permission [11]. Copyright 2019, Wiley. (b) The SOEC devices with different configuration and appearances. Copied with permission [12]. Copyright 2017, Springer Nature. (c) Thermodynamics of CO_2 and H_2O reduction reactions. Copied with permission [14]. Copyright 2011, Elsevier. (d) Schematic representation of technology development potential of different electrolyzers. Copied with permission [15]. Copyright 2015, International Energy Agency.

electrolyte restricts its durable application at higher temperature (*e.g.*, >80 °C). PEMECs utilize a solid polymer electrolyte with trifunctionality for proton conduction, electrolyzed gases separation, and electronic conduction suppression. Although it can migrate the challenge of low current density of AECs, the high price and vulnerability of proton exchanged membrane still hinder its large-scale industrialization. Compared to the former two counterparts, SOECs have unique advantages of cell robustness, low manufacture cost and unrivaled electrolysis efficiency [8].

SOECs were originally proposed in the mid-1960s as a technique of electrolysis of CO_2 for oxygen regeneration in the US manned spaceflight programs. In the mid-1990s, Sridhar *et al.* [9] proposed to use CO and O_2 produced by solid oxide cell in electrolytic mode during the day to generate electricity in fuel cell mode at night. Since the beginning of the 21st century, research groups around the world have been committed to developing novel materials to improve the performance and durability of stacks and reduce the production cost of syngas [10].

The ideal green energy scenarios incorporating SOEC is demonstrated by Song *et al.* and shown in Fig. 1 [11]. SOECs can not only split steam (H_2O) into H_2, but also electrolyze CO_2 to CO. More appealingly, the co-electrolysis of H_2O/CO_2 toward synthetic gas (mixture of H_2/CO) enables the integration of SOEC with a wide range of downstream chemical processes such as Fischer-Tropsch synthesis, enhancing the total energy efficiency. A representative SOEC device displays an all-solid lamellar-structure layout with three main components: a porous cathode (fuel electrode) where the reduction reaction (*e.g.*, CO_2 to CO and H_2O to H_2) happens with electrons flowing in, a porous anode (air electrode) where the oxidative reaction (O^{2-} to O_2) happens, and a dense electrolyte in the middle for ion transportation. From the perspective of configuration, SOEC could be classified into electrode (anode or cathode)-support, electrolyte-support and metal-supported ones. And the appearance of the electrolyzer could be either tubular, planar or flat-tubular shape (Fig. 1b) [12]. Furthermore, the operation of device in a reversed mode, named SOFC mode, is able to take advantage of the produced fuel (synthesized in SOEC mode) to generate electricity, while the power grid is on heavy demand [13].

SOEC can only properly work at elevated temperature (*e.g.*, >500 °C), which brings the incomparable merits from both thermodynamic and kinetic aspects. As the electrolysis temperature increases, the theoretical electrolysis voltage (electrical energy demand) gradually decreases for either CO_2 (blue line) or H_2O (red line) splitting processes (Fig. 1c), following the Eq. 1 shown below [14]. This feature enables the electrical energy saving over 20%-30%, while compared to AECs and PEMECs operated below 200 °C [15].

$$E_T = E_0 + \frac{\Delta S}{nF}(T - T_0) \quad (1)$$

Furthermore, the higher working temperature signifies the accelerated reaction kinetics, endowing the enhanced electrolysis current and conversion rate. For example, an SOEC for water splitting can generate a current density of ~1.5 A/cm^2 at a voltage less than 1.3 V, while the PEM electrolyzer required a much higher voltage of 1.6 V to generate a smaller current density of 1 A/cm^2 [16]. Such kinetics preponderance of SOEC is even more straightforward on sluggish CO_2 electrolysis. The SOEC for CO_2 reduction can easily reach a current density over 1 A/cm^2 with the overpotential less than 0.45 V and faradaic efficiency over 95%. While it is extremely difficult for the low temperature electrolyzer to

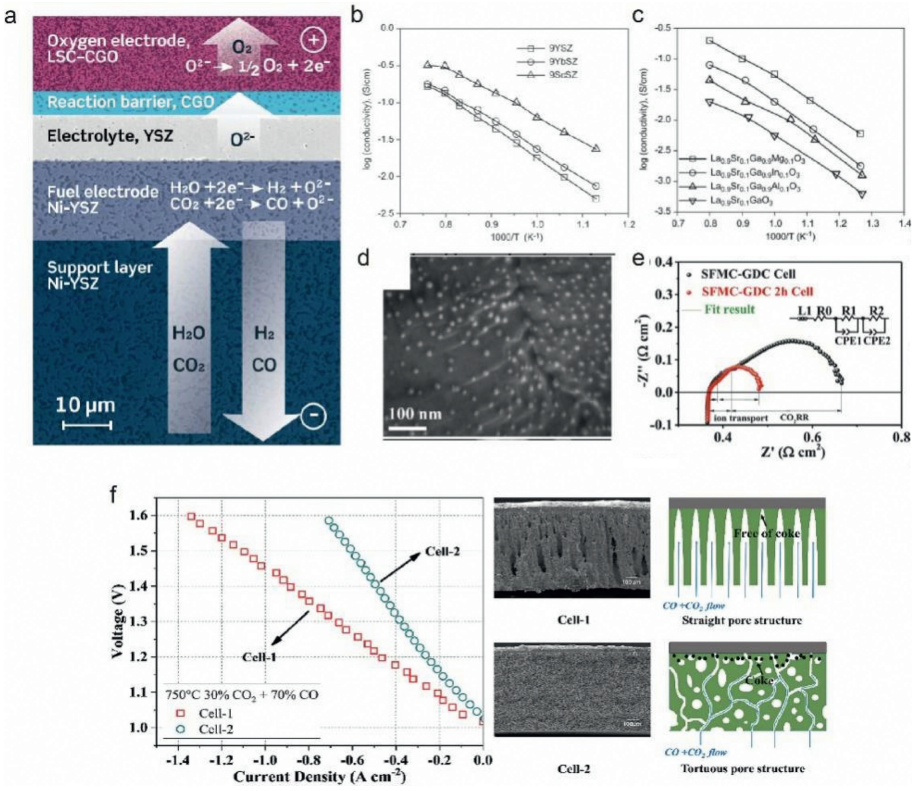

Fig. 2. (a) The configuration schematic of solid oxide electrolysis cell (SOEC) with supported cathode layer, fuel cathode layer, electrolyte, buffer layer and anode layer. Copied with permission [21]. Copyright 2020, Springer Nature. (b) The temperature dependent ionic conductivity plot of doped ZrO_2. Copied with permission [27]. Copyright 2022, The American Ceramic Society. (c) The temperature dependent ionic conductivity plot of doped LSG samples. Copied with permission [30]. Copyright 1994, American Chemical Society. (d, e) The SEM image of Co-doped $Sr_2Fe_{1.5}Mo_{0.5}O_{6-\delta}$ (SFMC) reduced for 2 h and the EIS plot for SFMC before and after exsolution for CO_2 electrolysis at 1.6 V and 800 °C. Copied with permission [66]. Copyright 2020, Wiley. (f) polarization curve and SEM image comparison of cell with straight pore and tortuous cathode decorated SOECs. Copied with permission [86]. Copyright 2022, Elsevier.

reach over 500 mA/cm^2 with the maintenance of Faradic efficiency over 60% [17]. Moreover, the all-solid nature of SOEC has granted the device superior retention for long-term operation. The CO_2-to-CO electrolysis technology developed by Haldor Topsøe, Demark, demonstrated a prolonged measurement for almost 8000 h with an acceptable degradation rate of 16 mV per 1000 h [18], which is more than one order of magnitude higher than that of the state-of-the-art low temperature analogue [19]. In Sep. 2022, the Board of Topsoe has decided to start the construction of the world's largest SOEC electrolyzer with the capacity of 500 MW/year in Denmark. The superiorities in activity and durability further strengthens the industrialization potential of SOEC in regard to reduced operating and capital costs per electrolyzer unit.

2. Single cell level

2.1. Electrolyte

The exploration of highly performed and stable single SOEC cell is the first milestone of commercialization. According to the different ionic conducting mechanisms, two types of SOECs, using oxygen ion conducting electrolyte (O-SOEC) and proton-conducting electrolyte (P-SOEC), were comprehensively studied, respectively [20]. For O-SOEC, the CO_2 or H_2O molecules receive electrons to produce CO or H_2, respectively. And the stripped oxygen ions are driven by the electric field and transported into anode chamber *via* electrolyte. The accumulated O^{2-} in anode are catalyzed to form O_2 and spontaneously release electrons (Fig. 2a) [21]. While in P-SOEC, the splitting of H_2O can only occur in anode to directly generate O_2 and the protons are transported into cathode to form H_2. The CO_2 electrolysis in P-SOEC is slightly more complicated, which requires the assistance of H_2O or H_2 splitting in anode [22,23]. However, the activation energy of temperature-dependent proton conducting is usually lower than that of ionic conducting, enabling the possibility to realize high efficiency electrolysis at intermediate temperature region [24].

The ideal electrolyte should possess good sinterability, high ionic conductivity and negligible electronic conductivity. Currently, two types of oxide with fluorite structure and perovskite structure were extensively employed as potential oxygen ion electrolytes in SOEC, respectively. The aliovalent cation doped ZrO_2 is the most commonly used electrolyte material in reversible solid oxide cell. The pure ZrO_2 demonstrates cubic structure only above 2370 °C, which showed highest conductivity among the derivates with other phases [25]. In order to stabilize such highly desired structure, low valence elements of Y^{3+} and Sc^{3+} are doped into ZrO_2, which further promoted the ionic conductivity through vacancy hopping mechanism. The 8 mol% Y doped ZrO_2 shows a high ionic conductivity of ~0.03 S/cm at 800 °C [26]. However, its high activation energy for ionic transportation significantly restricted the application potential at lower temperature (Fig. 2b) [27]. The Sc doped ZrO_2 demonstrates an enhanced conductivity over > 0.08 S/cm at 800 °C. But the high price of Sc is still the bottleneck for practical application [28]. The doped ceria (such as Gd or Sm doped CeO_2, (GDC, SDC)) presents higher ionic conductivity than doped ZrO_2 while the operation temperature below 600 °C. However, while exposed to reducing atmosphere in cathode of SOEC, the emergence of Ce^{3+}/Ce^{4+} redox pair in doped ceria leads to the electronic current leakage, the short-circuit of cell and lower faradic efficiency [29]. The Sr and Mg co-doped $LaGaO_3$ perovskite

($La_{0.9}Sr_{0.1}Ga_{0.8}Mg_{0.2}O_{3-x}$, LSGM) showed an outstanding ionic conductivity of 0.17 S/cm at 800 °C (Fig. 2c) [30]. However, the LSGM still suffers from the challenges of possible side-reaction with conventional Ni electrode to form less-conducting phase, and La diffusion into electrode to form catalytically inert phase [31].

Lowering the operating temperature of proton conductor can not only broaden the selection of sealant and interconnect components, but also simplify the downstream purification process of electrolysis products (*e.g.*, dry H_2 for steam electrolysis) [32]. Usually, one of the most predominant factor affecting proton conduction is the hydration capability and quantity of oxygen vacancy. While exposed to vapor for example, the water molecules are incorporated into surface oxygen vacancies to create two $^{\bullet}OH$. The barium cerates of $Ba(Zr_{0.1}Ce_{0.7}Y_{0.2})O_3$ (BZCY) [33] and $BaCe_{0.5}Zr_{0.3}Y_{0.16}Zn_{0.04}O_{3-d}$ (BCZYZ) [34] exhibited high proton conductivity. The additive of Zn, Cu, Ni and Fe were reported to enhance the sinterability of this series of proton conductor. However, they all suffers from the decomposition in H_2O- or CO_2-containing atmospheres. The common SOEC reactants, shorten their lifetimes. Alternatively, a hybrid ion conductor of $BaZr_{0.1}Ce_{0.7}Y_{0.2-x}Yb_xO_{3-\delta}$ (BCZYYb) has been developed and regarded as most promising electrolyte candidate for H-SOECs because of its high conductivity and stability even treated the critical condition of 50% H_2-50% H_2O or 50% H_2-50% CO_2 for over 300 h [24,35]. Duan *et al.* demonstrated the desirable stability of BCZYYb-based H-SOECs for 1200 h at 600 °C with the degradation rate of 30 mV per 1000 h [32]. Yet, the extremely high concentration of H_2O and CO_2 still lead to the gradual deposition of BCZYYb [36], indicating the huge room for future exploration of better proton conductor.

2.2. Fuel electrode (CO_2, H_2O)

The cathode in SOEC is the place where CO_2 and H_2O were reduced to target products, regardless of the type of electrolyte utilized. The material candidates for cathode must have high electrical conductivity, electrocatalytic activity, chemical stability/combability with the electrolyte, as well as economic/manufacture feasibility [37]. The Ni-cermet (mixture of Ni and electrolyte (*e.g.*, Y_2O_3 stabilized ZrO_2 (YSZ)) is currently the commercial cathode in SOEC, in which Ni phase provides electronic conducting pathway and reactive sites, and the electrolyte supplies ions transported from anode sides [38]. The electrochemical reduction will only happen at the triple phase boundary where Ni, electrolyte and reactant gases meet each other. During CO_2 electrolysis, some researchers thought it is necessary to add the reductive gas such as CO or H_2 to prevent the oxidation of Ni-YSZ by weak oxidants of CO_2 [39]. However, these protective gases will dilute the reactants concentration and decrease the electrolysis performance. Some other studies claimed the superfluousness of protective gas since the negative cathodic potential guarantees the electrons enriched environment on cathode to avoid the deep oxidation [40]. Unlike H_2 without carbon atom, the usage of CO as protective gas will inevitably bring another challenges of carbon deposition, stemming from the electroreduction of carbon species at the high electrolysis voltage and Boudouard reaction while the CO concentration is above the reaction threshold. The as-form carbon deposition could exist in the form of amorphous, graphite or carbon tube, blocking the active sites and degrading the devices [41]. Compared on Ni-YSZ, despite the Ni-BCZY cermet in P-SOEC exhibits better performance at intermediate temperature region, the poor redox stability and mechanical strengthen in highly humidified and reductive atmosphere are still obstacles needed to be resolved [42].

Alternatively, perovskite oxide cathode candidates with regular formula of ABO_3 have attracted much attention because of its earth abundance, mixed ionic and electronic conductivity and excellent redox stability. However, the superficial surface of perovskite is usually dominated by catalytically inactive A-O terminal with limited amount of oxygen vacancies, and B-cation enriched region is buried beneath the surface, restricting the performance of the cell [43]. Therefore, diverse intrinsic/extrinsic material engineering methodologies are developed to improve the electrocatalytic activity of the perovskite-related oxides.

Aliovalent cation doping is a very effective way to tune the structural properties and electronic configurations of perovskites, and further influence their electrocatalytic activities. The perovskite $SrFeO_{3-\delta}$ has a narrowed bandgap of ~2.0 eV, expressing good electrical conductivity but poor activity toward CO_2 splitting. The infiltration of Ni nanoparticles (NPs) significantly enhanced the CO_2 electrolysis performance with long-term stability for 100 h and 8 redox cycles [44]. Another example of electronic conducting $La_{0.2}Sr_{0.8}TiO_3$ (LST) also stressed the important role of doping effect. The doping of Mn into B-site of LST ($(La_{0.2}Sr_{0.8})_{0.9}(Ti_{0.9}Mn_{0.1})O_{3-\delta}$ (LSTM)) can create sufficient oxygen vacancies and enhance ionic conductivity. The material demonstrated desirable redox stability between SOFC mode (800 °C in a 5% H_2/Ar) and SOEC mode (1.4 V, CO_2, 800 °C) [45]. Vanadium (V) substituting $La_{0.5}Sr_{0.5}FeO_{3-\delta}$ was also shown to have enhanced content of oxygen vacancies which facilitates the CO_2 absorption. The 0.05 mol% of V doped into $La_{0.5}Sr_{0.5}Fe_{1-x}V_xO_{3-\delta}$ enhanced the CO_2 electrolysis current density by 51.2% at 1.6 V and 800 °C [46].

The wet impregnation is another widely used method to load active components onto oxide scaffold [47]. Loading of 2 wt% Fe_2O_3 on LSCM electrode was showed to drastically enhance the CO_2 electrolysis current by 75% at 800 °C, which could deliver a stable current of 0.36 A/cm^2 at 2 V [48]. Carneiro *et al.* reported that metal oxophilicity (metal-oxygen bond strength) was strongly correlated to the CO_2 activation and electrode deactivation processes, which can explain why the electrode with infiltrated Fe has better performance than those with Pd and Ni [49]. Ni, Cu and Ni Cu metals are successfully incorporated into LSCM porous framwork, and the comparison of electrochemical measurements showed that the NiCu-LSCM composite cathode had best activity of 0.782 A/cm^2 at 1.6 V and 800 °C) with high robustness for 100 h and ~10 redox cycles [50]. Besides metal, the $MnCo_2O_4$ spinel oxide were also reported to be impregnated into GDC skeleton with uniform distribution and served as electrode for SOEC. The current density for pure CO_2 electrolysis was able to reach 0.75 A/cm^2 with applied voltage of 1.5 V at 800 °C [51].

Within the last decade, an alternative electrode design principle, called *in-situ* exsolution, emerged and was capable to resolve the weaknesses of poor metal (or alloy)/oxide adhesion, uneven distribution and fabrication complexity possessed by impregnation. Briefly, the catalytically active elements were uniformly incorporated into the lattice of perovskite scaffold during first-step annealing, and then reduced, segregated and anchored onto the surface of oxide support [52]. The anomalous catalytic interface of emergent metallic/alloy nanoparticles embedded in oxide parent displays uniform dispersion, enhanced stability. Intensive researchers have discovered both internal and external manipulation parameters to boost thermodynamic and kinetic of exsolution process. For instance, the point non-stoichiometry in lattice [53], topotactic ion exchange [54] and lattice strain [55] were applied to enhance the quality of exsolved particles. And the electrochemical poling method also facilitated the exsolution by creating transit ultra-low oxygen partial pressure (P_{O_2}) [56]. Using $La_{0.75}Sr_{0.25}Cr_{0.5}Mn_{0.5}O_{3-\delta}$ (LSCM) scaffold as an example again, the exsolved Ni nanoparticles decorated LSCM electrode demonstrated an current density rise from 0.27 A/cm^2 to 0.38 A/cm^2 at 2.0 V and Faradaic efficiency enhancement by 60% [57]. On the case of $La_{0.4}Sr_{0.4}Fe(\text{or Ni})_{0.06}Ti_{0.94}O_{2.97}$, Tsekouras *et al.* evidenced that the presence of electrocatalytically active exsolved Fe or Ni nanoparti-

cles and co-generated oxygen vacancies dramatically lowered the activation barrier to steam electrolysis (900 °C, 47% H_2O and 53% N_2) compared to pristine perovskite [58]. Moreover, the Ni-Fe, Fe-Co and Ru-Fe alloy were also reported to exsolve from various perovskite scaffolds [59–65], which not only have superb electrolysis activity, but also deliver enhance coking resistance. Also, the reduction temperature and duration are also key parameters influencing morphology of exsolved particle, further the electrolysis performance (Figs. 2d and e) [66]. The plenty of theoretical simulation results proved the preferable absorption and activation of reactant at exsolved metal-support interface. And the as-formed oxygen vacancies adjacent to these interfaces can also contributed to the enhanced charge carrier transfer kinetics, collectively facilitating the overall electrolysis process.

2.3. Air electrode

The anodic reaction for typical SOEC is often the sluggish 4-electron involving oxygen evolution reaction (OER), which has a redox potential of 1.229 V (*vs.* SHE) and occupies the majority energy consumption of SOEC. Therefore, the development of novel anode materials with minimized overpotential is crucial for highly efficient SOEC [67,68]. The first generation of anode electrode is Sr doped $LaMnO_3$ perovskite (LSM) which had also been applied for SOFC for decades [69]. The electronic conducting characteristic of LSM (over 100 S/cm at 800 °C) [70] determines that it has to be well mixed with ionic conducting electrolyte materials (YSZ, GDC) to form mixed ionic and electronic conducting composite [71], and the reaction can only happen at the triple phase boundary (TPB) where LSM, electrolyte and gas meet.

The poor intrinsic activity of LSM motivates the development of second-generation air electrode of $La_{0.6}Sr_{0.4}Co_{0.2}Fe_{0.8}O_3$ (LSCF) perovskite which has a reasonable electronic conductivity of 200-300 S/cm, but an orders of magnitude higher ionic conductivity of 0.01-0.1 S/cm. Therefore, the TPB length can be substantially extended to the whole air electrode region, which enhances the reaction kinetics even without the mixture of electrolyte [72]. Recently, other types of oxide were also developed to broaden the family of air electrode. The Ruddlesden-Popper (RP) structure oxide such as rare earth nickelate of Nd_2NiO_4 [73], usually demonstrate a higher oxygen ionic conductivity than that of simple perovskite by several orders of magnitudes, owing to the highly anisotropic interstitial diffusion mechanism of oxygen ion on the *a*-*b* plane, confirmed by Molecular dynamics (MD) simulation on La_2NiO_4 [74]. Beyond simple perovskite, the double perovskite of $AA'BB'O_{6-\delta}$ with the AO-BO_2-AO-BO_2 stacking along *c*-axis have shown outstanding oxygen surface exchange coefficient and ionic diffusion rates. MD results showed that oxygen ions migrated in $PrBaCo_2O_{5.48}$ [75] and $GdBaCo_2O_{5+x}$ [76] were also highly anisotropic. The widely studied fuel electrode of $Sr_2Fe_{1.5}Mo_{0.5}O_{6-\delta}$ (SFM) was also found to be efficient as air electrode with the polarization resistance is only 0.26 Ω cm^2 at open-circuit condition, and the electrolysis current density at 1.3 V reaches 0.88 A/cm^2 At 900 °C, which was better than that of the LSM-YSZ anode [77]. The cell with $PrBa_{0.5}Sr_{0.5}Co_{1.5}Fe_{0.5}O_{5+\delta}$ (PBSCF) double perovskite anode can deliver the maximum current density of 1.3 A/cm^2 is obtained at 1.3 V and humidity of 50% at 800 °C. And the cell exhibited excellent durability of 120 h and good reversibility [78,79].

2.4. Buffer layer

Upon prolonged operation for thousands of hours, the significant ion inter-diffusion between different components will lead to the formation of insulating phase, resulting in the deactivation of electrolysis stack. The unwanted reactions between electrode and electrolyte can be alleviated by adding the buffer layer between them. For example, LSCF is one of the most promising air electrodes for O-SOEC, which however, will react with YSZ electrolyte to form $SrZrO_3$ and $La_2Zr_2O_7$ insulating phases [80]. Thereby, doped ceria with comparable ionic conductivity as YSZ was usually used as a buffer layer to avoid the undesired reaction between the LSCF-based electrode and YSZ electrolyte. Lyu *et al.* used one-pot hydrothermal method to prepared LSCF@GDC twined hybrid which showed a 40-fold promoted performance under oxygen starving conditions, compared to bare LSCF at 750 °C, suggesting that the additive of buffer layer component can also facilitate the oxygen activation kinetics. Nevertheless, the additive of GDC will unavoidably decrease the total conductivity of LSCF and enhance the total ohmic resistance of the cell [81]. Besides YSZ, another commonly used electrolyte of LSGM will react with Ni cermet to form lanthanum nicklates which is catalytically inert for fuel activation. Consequently, again, a buffer layer of doped ceria has to be incorporated between the Ni cermet and LSGM electrolyte to resolve this problem [82].

2.5. Microstructure engineering

The microstructure engineering of the specific component, especially electrode, of SOEC is equally vital as the material selection, which is essentially correlated to the mass/heat transportation and the lengthen of TPB. Typically, the fuel electrode of the mixture of Ni and YSZ has high porosity over 40% which is created by the additive of pore maker during fabrication. The high active surface area due to porous structure of electrodes could guarantee the sufficient exposed active sites on which the reactants meet. Unlike graphite and potato starch which generates coarser and uneven pores, respectively, the PMMA can generate much finer pores, leading to enhanced electrochemical performance. The SOEC using PMMA as pore former shows a highest electrolysis at −713 mA/cm^2 at 1.3 V and 800 °C with a stable operation for over 400 h [83]. Liu *et al.* disclosed the optimum PMMA content of 10 wt% in cathode fabrication, resulting in a high porosity of 45% and electronic conductivity of 6726 S/cm [84]. Alternatively, the porous framework manufacture and deposition of catalytic site can be done by two separated steps. For example, Fan *et al.* reported the construction of ionic conductive YSZ matrix concomitantly with the dense electrode. And then the LSCF catalytic air electrode compound could be introduced by impregnation to form TPB. However, the agglomeration of LSCF was observed after 8 charged/discharged cycles, responding for its unsatisfied redox stability [85]. The manipulation of morphology of pore can not only boost the electrolysis efficiency, but also migrate the challenges confronted in extreme condition. Li *et al.* reported that the modification of tortuous pore to finger-like straight pore can enhance the carbon deposition resistance of the SOEC for CO_2 conversion. The critical current density at which coking starts to occur was found the be enhanced from 0.5 and 1.0 A/cm^2 to 1.0 and 1.5 A/cm^2, respectively. The electrochemical impedance spectroscopy (EIS) results disclosed that straight pore paths accelerate the removal of as-produced CO to suppress the Boudouard reaction (Fig. 2f) [86]. The microstructure engineering was also employed to alleviate the delamination of electrode/electrolyte interface during SOEC/SOFC cycling [87]. Khan *et al.* added a SSZ porous layer between the dense SSZ electrolyte and the porous LSM air electrode and found that electrolysis current density increased from 294 mA/cm^2 to 407 mA/cm^2 after 5 cycles at 1.3 V in 10% H_2O-90% H_2, at 800 °C, owing to the raised quantity of TPB and migrated high oxygen partial pressure. In comparison, The cell without such porous buffer layer suffered from the formation of insulating zirconate phase, LSM aggregation and undesirable silver deposition [88].

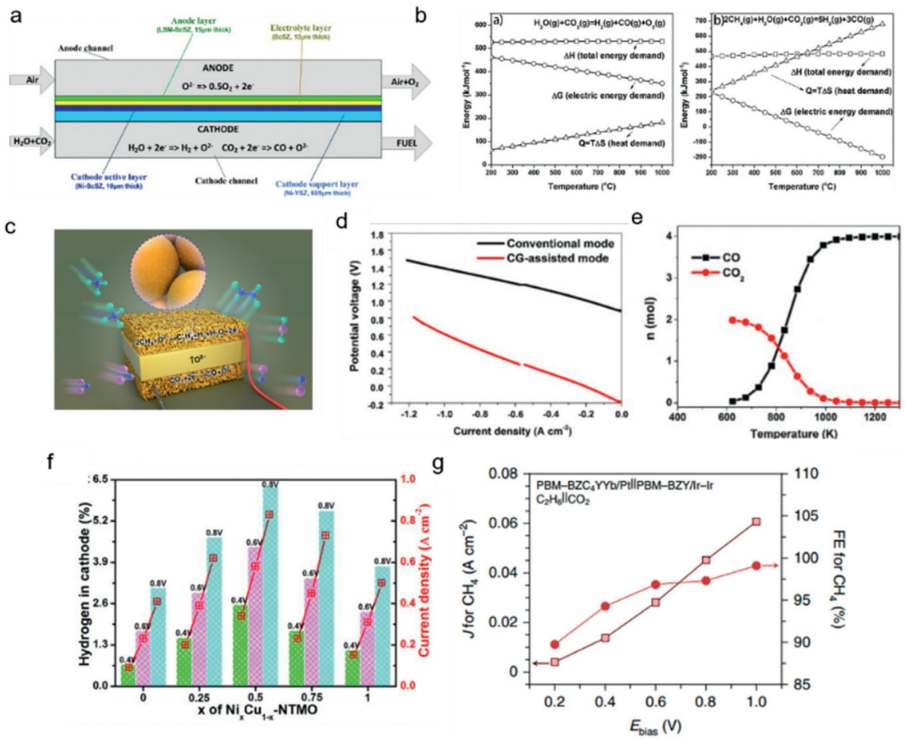

Fig. 3. (a) The model of CH_4 assist-SOEC. Copied with permission [89]. Copyright 2016, Elsevier. (b) The calculated energy consumption for conventional H_2O/CO_2 co-electrolysis and CH_4 assisted electrolysis. Copied with permission [89]. Copyright 2016, Elsevier. (c) The schematic of CH_4 oxidative coupling assisted CO_2 electrolysis. Copied with permission [65]. Copyright 2018, Wiley. (d) The polarization curves of conventional SOEC and carbon gasification assisted SOEC at 850 °C. Copied with permission [93]. Copyright 2016, Elsevier. (e) The calculated thermodynamic equilibrium results for the reaction of 2 mol O_2 with 98 mol carbon at different temperatures. Copied with permission [93]. Copyright 2016, Elsevier. (f) The amount of H_2 depends on the current in the cathode in C_2H_6 dehydrogenation assisted P-SOEC. Copied with permission [94]. Copyright 2020, American Chemical Society. (g) CH_4 partial current density and partial Faradaic efficiency in C_2H_6 dehydrogenation assisted P-SOEC. Copied with permission [95]. Copyright 2020, Springer Nature.

2.6. Operation optimization

2.6.1. Fuel-assisted O-SOEC

Now that the electricity accounts for a majority of total energy consumption of SOEC, the cheap low-carbon molecules were added into anode chamber to modify the elementary reaction happening on electrode, aiming to lowering the overpotential for electrolysis. The CH_4-assisted SOEC by coupling CH_4 in air electrode was systematically modeled by Ni's groups on 2016 (Fig. 3a) [89]. It was shown that the introduction of CH_4 in anode of CO_2/H_2O co-electrolysis device effectively lower the equilibrium potential of SOEC (Fig. 3b), and thus decrease the electricity consumption. The reaction can be triggered even at the low potential of 0.2 V at 750 °C, and the device could realize the co-generation of electricity and syngas at the current density less than 600 A/m^2 and at 850 °C.

To enhance the total productivity and efficiency of fuel-assisted SOEC, the highly selective catalyst were facilely prepared to convert CH_4 to valuable syngas *via* partial oxidation of methane (POM) reaction [90]. The total electrical energy consumed of the POM-assisted SOEC for the CO_2/H_2O co-electrolysis is decreased compared with that of the convenient SOEC. An electrolysis current of 350 mA/cm^2 can be obtained at a cell voltage of only 0.4 V in the POM assisted mode. Following this line of thinking, Lu *et al.* developed the Ni Cu alloy exsolved LSCM electrode and assembly the CH_4-assist SOEC to efficiently reform of CH_4/CO_2 to produce syngas by an electrochemical way. It was found that the cell can reach the current density to 1.2 A/cm^2 at 1.5 V and the productivity of CO is highly dependent on the Ni:Cu ratio in alloy (Fig. 3c). The cell demonstrated no obvious degradation after 300 h of high-temperature operation and 10 redox cycles [65].

By optimizing the catalyst in electrode, the methane can be electrochemically converted to ethylene in SOEC *via* an oxidative coupling reaction. On a Fe exsolved $Sr_2Fe_{1.5+x}Mo_{0.5}O_{6-\delta}$ electrode, the concentration of C_2 in anode outlet can reach 16.7% with total selectivity over 80% and CH_4 conversion rate over 40%. This process realizes a stable output for 100 h and 10 redox cycles, suggesting its potential for practical application [91]. While replacing CH_4 with C_2H_6, more value C_{2+} products can be expected *via* the advanced electrochemical-thermal coupling catalytic process. This design was realized by Song *et al.* by the impregnation of γ-Al_2O_3 onto the surface of $La_{0.6}Sr_{0.4}Co_{0.2}Fe_{0.8}O_{3-\delta}$-$Sm_{0.2}Ce_{0.8}O_{2-\delta}$ (LSCF-SDC) anode in an O-SOEC. Usually, the thermal oxidative dehydrogenation of ethane is challenged by the deep oxidation, resulting in low selectivity. In comparison, in Song's work, a high ethylene selectivity of 92.5% and ethane conversion of 29.1% at 600 °C can be observed [92]. The infiltrated Al^{3+} was bonded to Fe *via* an Al-O-Fe structure and enriched the state density around Fermi level of Fe, facilitating the conversion of C_2H_6. Besides gaseous fuel, the solid carbon can also be employed to promote the activity of SOEC in which the oxidation of carbon is predominant reaction in anode. The theoretical overpotential of C-assist CO_2/H_2O co-electrolysis can be reduced by about 1 V at 850 °C, compared to traditional analogues (Figs. 3d and e). The thermodynamic equilibrium calculation further proved that CO is the main product while the operation temperature was over 550 °C, suggesting its good combability with high temperature electrolysis [93].

2.6.2. Fuel-assisted P-SOEC

As mentioned above, the P-SOEC can migrate the biggest weakness of poor intermediate temperature performance of O-PCEC, offering brighter potential for industrialization. Moreover, for the

fuel-assist SOEC, the proton conducting mode without existence of oxygen species in anode, providing an alternative way to realize the co-generation of dehydronated and hydrogenated products in separated chambers. Zhang *et al.* reported an electrolysis of CO_2 in a P-SOEC with the electrochemical conversion of C_2H_6 to C_2H_4 in anode. The Ni_xCu_{1-x} alloy exsolved $Nb_{1.33}(Ti_{0.8}Mn_{0.2})_{0.67}O_{4-\delta}$ anode showed improved stability and high coking resistance for 10 h with the highest ethane conversion of 75.2% and ~100% ethylene selectivity at 0.8 V (Fig. 3f). The CO_2 was both directly reduced to CO and involved into the reversed water gas shift reaction on cathode, leading to a ~6.3% H_2 in the cathode outlet [94]. Using the same cell configuration with SDC supported Ir (SDC/Ir) electrode, Li *et al.* reported the achievement of selectivity over 95% toward CH_4 of electrochemical hydrogenation of CO_2 at 400 °C. Further enhancing the bias leads to the promoted CH_4 selectivity to reach almost 100%. The selectivity is strongly correlated to the stabilization of different transition state of carbon species, which is controlled by the Ir-O hybridization (Fig. 3g) [95].

On the other hand, the CO_2 electrolysis in P-SOEC mode can direct generate CH_4 with the assist of H_2O splitting in anode. Pan reported that at an optimal low temperature of 450 °C and electrolysis current of 1 A/cm^2, a high CH_4 productivity of 34.6% can be achieved, which is much higher than the yield of thermocatalytic CO_2 methanation. Further enhancing the electrolyte thickness could improve the CH_4 yield to 40.9% by enhancing the faradic efficiency. And recycling the produced H_2 in anode could boosts the CH_4-yield ratio to 71.2%. Such high performance is not only due to low operating temperature, but also owing to the physical separation of the CO_2 and H_2O feedstocks. Such electrochemical CO_2 upgrading with PCECs is proved to be economically benign by the techno-economic analysis projects [96].

3. Stack level

Compared to individual cell, the SOEC stack brings more challenges beyond activity. The stacked cells compose single SOEC module which is the basic unit of SOEC system. Taking planar cell as an example, each individual cell is assembled into metallic frames, which is sandwiched by interconnect component with incurved flow channel. A sealant is simultaneously employed to prevent potential gas leakage or mixing. For steam splitting, the pre-purification system as well as gas storage system are usually required to purify the steam reactant and store H_2 product, respectively.

3.1. Interconnect

Since the Interconnects not only separate the gas in cathode and anode, but also provide the electrical conduction pathway ways among all stacks, the qualified interconnect should be stable in reductive, oxidative and moisture atmospheres. The chromic based perovskites such as $LaCrO_3$ could serve as potential interconnect due to its high chemical and thermal stability. However, its high cost for manufacture restricts its commercialization. In comparison, the high-chromium (Cr) containing steels (430, 441, *etc.*) are the alternatives owing to its economic efficiency, promoted mechanical strength, and better thermal conductivity. Nevertheless, the high chromium content in steel resulted in deteriorate Cr vaporization and further diffusion into the cell, worsening the performance of the cell. To overcome this problem, these stainless steels are usually coated to slow down it degradation rate and minimize Cr poisoning on cell [97].

For example, the ChromLok^{TM} MCO-based composition $(Mn, Co)_3O_4$ is applied to Crofer 22 APU stainless steel for O-SOEC stack for over 700 h. The MCO coating is found to decrease the oxidation rate by about one order of magnitude, and decrease the Cr evaporation rate by fourfold [98]. On the other hand, the $(Co, Mn, Fe)_3O_4$ spinel oxide coated Crofer 22 APU stainless steel successfully operated for over 40,000 h. Due to the presence of vapor at high temperature, the coating in fuel side degraded faster than one in cathode side [99].

3.2. Sealant

Unlike tubular SOEC with great spatial separation of fuel and air, the SOEC with planar configuration takes higher risk of potential gas leakage. the sealants for a SOEC stack should be chemically, mechanically and thermally stable under harsh working conditions. Further, reactivity between sealant and interconnect has to be as low as possible. The noble metals are chemically inert and have good elasticity. However, they are usually extremely expensive. Glass and glass-ceramic composite seals such as borosilicates, or alkaline earth metal oxides containing silicate or borosilicate glasses, exhibit much higher cost efficiency [100]. Nevertheless, upon prolonged measurement, it is universally found that the silica-containing impurities diffused from sealant into cell can block the electrocatalytically active sites, inevitably cause degradation and lead to increased polarization resistance [101].

3.3. System operation

To improve the electrolysis production rate and decrease degradation of the cell, the endeavors have to be devoted to optimize the operation conditions of the stacks, which is usually ignored for button cell measurement. Xu *et al.* reported the effect of the flows of hydrogen electrode (Figs. 4a and b), water pressure, and electrolysis current density on the performance of stack composited by a 30-layer single cell of NiO-YSZ/NiO-YSZ/YSZ/LSM-YSZ with an active area of 63 cm^2. High flow and low electrolysis current density are beneficial to increase electrolysis efficiency and reduce conversion (Fig. 4c). The speculated reason is that the heat generated from the stack internal resistance is much higher than that required for water decomposition at high current densities, leading to increases in the operating voltage. Under the output voltage 39 V (thermoneutral voltage), the current density increased from 0.185 A/cm^2 to 0.22 A/cm^2 with the water pressure increased from 70% to 90%. Besides, the degradation rate of the stack was 11.7% 1000 h^{-1} under current density 0.15 A/cm^2 and 80% water pressure at 800 °C, and the electrolysis efficiency decreased from 113% to 92%. The Post-mortem analysis revealed that both the oxygen and hydrogen electrode at inlet area were delaminated from the electrolyte (Fig. 4d), and the accumulation of Ni particles was obvious at the hydrogen electrode [102]. Xu *et al.* further improved the performance and long-term stability of the stack with a single layer by replacing the LSM-YSZ by an LSCF-GDC cathode. The LSCF-GDC stack exhibited a high hydrogen production rate with 159.2 Nml cm^{-2} h^{-1}, much higher than 99.5 Nml cm^{-2} h^{-1} of the LSM-YSZ stack under electrolysis voltage with 1.1 V at 800 °C. When it operated under 0.5 A/cm^2 at 750 °C for 640 h, the degradation rate of stack performance is 4.33%, which is better than that of LSM-YSZ at 4.89%. Besides, there was no significant flaking of the LSCF electrode after the test (Fig. 4e) [103].

Regarding interconnector, O'Brien *et al.* found that Cr poisoning can seriously affect the performance of the cell in contact with the Inconel collector, the total degradation rate of the stack with 10-layer NiO-YSZ/YSZ/LSCF is 8.9% K/h under 0.2 A/cm^2 and 70% H_2O at 800 °C, where the degradation rate of the top cell is 26.8% and that of other cells is 3.7% (Fig. 4f) [104]. To prevent the electrode from being corroded, the LSM and $MnCo_{1.9}Fe_{0.1}O_4$ (MCF) materials were used as an electrode protection layer [105,106]. Fang *et al.* applied the MCF as a protection layer between the LSCF oxygen electrode and the connector, the degradation rate

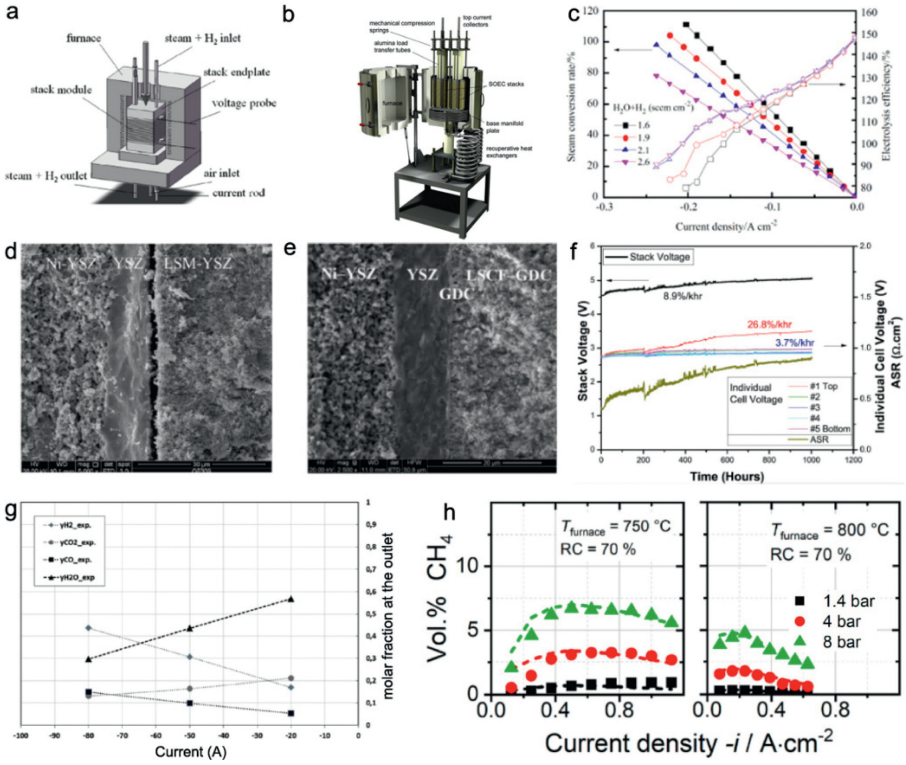

Fig. 4. (a, b) 3D view of the stack module mounting. Copied with permission [102]. Copyright 2014, Elsevier. (c) Effect of different flows on the hydrogen electrode on the steam conversion rates and electrolysis efficiencies of the stack module at 800 °C and a constant 80% H_2O-20% H_2. Copied with permission [102]. Copyright 2014, Elsevier. (d, e) SEM images of the cross-section (fracture surface) of the Ni-YSZ/YSZ/LSM–YSZ and Ni-YSZ/YSZ/GDC/LSCF-GDC cells after electrolysis at air inlet area. Copied with permission [102,103]. Copyright 2015, Elsevier. (f) Stack with NiO-YSZ/YSZ/LSCF cell test 1000 h at 0.2 A/cm^2 in electrolysis mode. Copied with permission [104]. Copyright 2013, Elsevier. (g) Gas outlet measurements of the 10-cell stack at 800 °C with cathodic inlet: 65% H_2O-25% CO_2-10% H_2 with conversion rate of oxidized species is 32% at 0.5 A/cm^2. Copied with permission [107]. Copyright 2015, Elsevier. (h) Gas analysis of the CSC and the ESC stack according to the steady state co-electrolysis experiments. Copied with permission [108]. Copyright 2020, Elsevier.

of the stack is only 0.7%/1000 h under 0.5 A/cm^2 and 50% H_2O at 800 °C, indicating high stability of stack with protection layer [106].

The O-SOEC stack could be also applied to the co-electrolysis mode of H_2O and CO_2. Mougin *et al.* performed co-electrolysis using a stack with 10-layer NiO-YSZ/YSZ/GDC/LSC single cell under 65% H_2O-25% CO_2-10% H_2. A maximum current density with −0.8 A/cm^2 and gas conversion of 52% were obtained at 1.15 V at 800 °C. When the electrolysis current with 0.8 A/cm^2 was applied at 800 °C, the H_2-CO syngas production was 0.34 Nm^3/h, the O_2 production was 0.17 Nm^3/h, and no methane production was observed by chromatography (Fig. 4g), which is consistent with the thermodynamic prediction, proving the feasibility of the co-electrolysis at the stack [107]. Riedel *et al.* investigated the effect of pressure on the electrolysis performance of a stack with a 10-layer single cell, and compared the performance of the electrolyte support cell (ESC) and cathode support cell (CSC), where the structure of former was NiO-GDC/GDC/3YSZ/GDC/LSCF and the latter was NiO-YSZ/YSZ/GDC/LSCF. The co-electrolytic atmosphere was 60% H_2O-30% CO_2-10% H_2 and test pressure was 1.4, 4, and 8 bar, respectively. The current density of CSC was 0.75 A/cm^2 under electrolyte voltage of 1.3 V and pressure of 1.4 bar at 750 °C (Fig. 4h). The CH_4 yield increased from 2% to 7% with the external pressure increased from 1.4 bar to 8 bar under the electrolysis current 0.5 A/cm^2 at 750 °C, which is consistent with high pressure, high H_2/CO ratio, and low temperature is favorable for methanation reaction. Besides, Increasing the pressure could decrease the voltage of stack and increase the core temperature of stack for the methanation reaction is exothermic. In addition, the electrolytic current of ESC was only 0.3 A/cm^2 under 1.3 V at 800 °C and the maximum methane yield is only 5% for the higher internal resistance (Fig. 4h) [108].

4. Perspectives

In this review, we have briefly summarized the recent developments of SOEC technology mainly at cell and stack levels. Meanwhile, we have stressed that further optimization of various parameters of SOEC is still urgently required to further promote the overall activity and durability.

Both performance and cell durability have been improved drastically by order of magnitude in the past decade. The lifetime of the SOEC should be at least 50000 h to maintain its competitiveness in the market. Haldor Topsoe in Demark has commercialized the commercially competitive CO_2 electrolysis technology with lifetimes over 7000 h and degradation rate below 0.4% per 1000 h [109]. However, how to completely prevent Ni segregation and stability of Ni-YSZ fuel electrode (*e.g.*, resistance against moisture for steam splitting, or resistance against carbon deposition in CO_2 electrolysis), especially at the condition of high electrocatalysis current/voltage are still the long-lasting issues that should be addressed carefully. Moreover, the mechanical stability of the cell upon redox operation is still critical. Impregnating functional layers or anchoring Ni nanoparticles *via* exsolution could be the alternative resolutions. But how to transplant the promoting effect on button cell level to stack level is still challenging.

For O-SOEC, the operation of the cell by fuel assistant at anode can facilitate the thermodynamics of CO_2 electrolysis at cathode and simultaneously take full advantage of the generated oxygen molecules at anode to upgrade the alkanes to valuable products.

On the other hand, the basic working principle of the P-SOEC allows the generation of pure hydrogen without extra step for gas separation. The lower activation energy for proton diffusion determines its lower operation temperature than that of O-SOEC. Nevertheless, so far, the technology readiness level (TRL) of the P-SOEC is far lower than that of conventional O-SOEC, and no commercial stacks or systems has been demonstrated yet. The remaining challenges related to P-SOEC arise from both structures and materials employed in different stack/cell designs.

From the economical perspective, the total electrolysis products amount over the SOEC stack's lifetime directly determine the unit price (such as cost of 1 kg H_2). This core parameter will be compared to that of alkaline or PEM electrolyzers which directly determine its commercialization potential. Therefore, the optimization of operation condition of the stack (temperature, gas inlet, current, *etc.*) should be considered collectively to maximize its merits in respect of efficiency, and minimize the weakness in poorer reliability.

Declaration of competing interest

The authors declare that they have no known competing financial interests or personal relationships that could have appeared to influence the work reported in this paper.

Acknowledgments

This research was supported financially by the National Key Research & Development Program of China (No. 2018YFE0124700), the National Natural Science Foundation of China (Nos. 22272136, 22102135, 22202041, 22172129, 52072134, U1910209, 51876181 and 51972128) Science and Technology Projects of Innovation Laboratory for Sciences and Technologies of Energy Materials of Fujian Province (IKKEM) (No. HRTP-[2022]-23) and Hubei Province (Nos. 2021CBA149 and 2021CFA072). Y. Sun acknowledges the financial support from Guangdong Basic and Applied Basic Research Foundation (Nos. 2022A1515010069 and 2020A1515110904) and the Natural Science Foundation of Fujian Province (No. 2021J01212759).

References

[1] Z. Caineng, Y. Zhi, H. Dongbo, et al., Pet. Explor. Dev. 45 (2018) 604–618.
[2] J.E. Bistline, Joule 5 (2021) 2551–2563.
[3] K.O. Yoro, M.O. Daramola, CO_2 emission sources, greenhouse gases, and the global warming effect, in: K.O. Yoro (Ed.) Advances in carbon capture, Elsevier, New York, 2020, pp. 3-28.
[4] J.B. Hansen, Faraday Discuss. 182 (2015) 9–48.
[5] M.S. Ziegler, J. Song, J.E. Trancik, Energy Environ. Sci. 14 (2021) 6074–6098.
[6] D. Connolly, H. Lund, B.V. Mathiesen, Renew. Sust. Energ. Rev. 60 (2016) 1634–1653.
[7] M. Aresta, A. Dibenedetto, A. Angelini, Chem. Rev. 114 (2014) 1709–1742.
[8] Y. Tian, N. Abhishek, C. Yang, et al., Matter 5 (2022) 482–514.
[9] K.R. Sridhar, B.T. Vaniman, Solid State Ionics 93 (1997) 321–328.
[10] Y. Zheng, J. Wang, B. Yu, et al., Chem. Soc. Rev 46 (2017) 1427–1463.
[11] Y. Song, X. Zhang, K. Xie, et al., Adv. Mater. 31 (2019) 1902033.
[12] Y. Zhou, Study on Fabrication and Performance of Metal-Supported Solid Oxide Fuel Cells, Springer, Shanghai, 2017.
[13] D. Gu, G. Zhang, J. Zou, Chin. Chem. Lett. 32 (2021) 3548–3552.
[14] C. Graves, S.D. Ebbesen, M. Mogensen, K.S. Lackner, Renew. Sust. Energ. Rev. 15 (2011) 1–23.
[15] A. Körner, C. Tam, S. Bennett, Gagné, Technology roadmap-hydrogen and fuel cells, International Energy Agency, Paris, 2015.
[16] S. Shiva Kumar, V. Himabindu, Mater. Sci. Energy Technol. 2 (2019) 442–454.
[17] R. Küngas, J. Electrochem. Soc. 167 (2020) 044508.
[18] R. Küngas, P. Blennow, T. Heiredal-Clausen, et al., Progress in SOEC Development Activities at Haldor Topsøe, 2019.
[19] L. Wang, M. Chen, R. Küngas, et al., Renew. Sust. Energ. Rev. 110 (2019) 174–187.
[20] I. Zvonareva, X.Z. Fu, D. Medvedev, Z. Shao, Energy Environ. Sci. 15 (2022) 439–465.
[21] A. Hauch, R. Kungas, P. Blennow, et al., Science 370 (2020) eaba6118.
[22] X. Zhang, L. Ye, K. Xie, Energ. Fuel 36 (2022) 11576–11583.
[23] N. Shi, Y. Xie, D. Huan, et al., J. Mater. Chem. A 7 (2019) 4855–4864.
[24] L. Lei, J. Zhang, Z. Yuan, et al., Adv. Funct. Mater. 29 (2019) 1903805.
[25] M. Laguna-Bercero, J. Power Sources 203 (2012) 4–16.
[26] M. Ni, M.K. Leung, D.Y. Leung, Int. J. Hydrogen Energy 33 (2008) 2337–2354.
[27] D.W. Strickler, W.G. Carlson, J. Am. Ceram. Soc. 47 (1964) 122–127.
[28] K. Yamaji, H. Yokokawa, 8 - Oxygen ionic conductor, in: C.C. Sorrell, S. Sugihara, J. Nowotny (Eds.), Materials for Energy Conversion Devices, Woodhead Publishing, New York, 2005, pp. 212–234.
[29] H. Sumi, E. Suda, M. Mori, Int. J. Hydrogen Energy 42 (2017) 4449–4455.
[30] T. Ishihara, H. Matsuda, Y. Takita, JACS 116 (1994) 3801–3803.
[31] Z. Gao, H. Wang, E. Miller, et al., ACS Appl. Mater. Interfaces 9 (2017) 7115–7124.
[32] C. Duan, R. Kee, H. Zhu, et al., Nat. Energy 4 (2019) 230–240.
[33] N.L.R.M. Rashid, A.A. Samat, A.A. Jais, et al., Ceram. Int. 45 (2019) 6605–6615.
[34] L. Gan, L. Ye, S. Wang, et al., Int. J. Hydrogen Energy 41 (2016) 1170–1175.
[35] L. Yang, S. Wang, K. Blinn, et al., Science 326 (2009) 126–129.
[36] C. Duan, J. Tong, M. Shang, et al., Science 349 (2015) 1321–1326.
[37] X. Zhang, Y. Song, G. Wang, X. Bao, J. Energy Chem. 26 (2017) 839–853.
[38] Y. Zheng, Z. Chen, J. Zhang, Electrochem. Energy Rev. 4 (2021) 508–517.
[39] M. Chen, Y.L. Liu, J.J. Bentzen, et al., J. Electrochem. Soc. 160 (2013) F883–F891.
[40] Y. Song, Z. Zhou, X. Zhang, et al., J. Mater. Chem. A 6 (2018) 13661–13667.
[41] T.L. Skafte, Z. Guan, M.L. Machala, et al., Nat. Energy 4 (2019) 846–855.
[42] M.C. Tucker, Int. J. Hydrogen Energy 45 (2020) 24203–24218.
[43] J. Druce, H. Téllez, M. Burriel, et al., Energy Environ. Sci. 7 (2014) 3593–3599.
[44] C. Zhu, S. Hou, L. Hou, K. Xie, Int. J. Hydrogen Energy 43 (2018) 17040–17047.
[45] L. Ye, X. Hu, X. Wang, et al., J. Mater. Chem. A 7 (2019) 2764–2772.
[46] Y. Zhou, Z. Zhou, Y. Song, et al., Nano Energy 50 (2018) 43–51.
[47] Y. Niu, W. Huo, Y. Yu, et al., Chin. Chem. Lett. 33 (2022) 674–682.
[48] C. Ruan, K. Xie, L. Yang, et al., Int. J. Hydrogen Energy 39 (2014) 10338–10348.
[49] J. Carneiro, X.K. Gu, E. Tezel, E. Nikolla, Ind. Eng. Chem. Res. 59 (2020) 15884–15893.
[50] C. Zhu, L. Hou, S. Li, et al., J. Power Sources 363 (2017) 177–184.
[51] L. Zhang, Y. Tian, Y. Liu, et al., ChemElectroChem 6 (2019) 1359–1364.
[52] O. Kwon, S. Joo, S. Choi, et al., J. Phys. Energy 2 (2020) 032001.
[53] D. Neagu, G. Tsekouras, D.N. Miller, et al., Nat. Chem. 5 (2013) 916–923.
[54] S. Joo, O. Kwon, K. Kim, et al., Nat. Commun. 10 (2019) 697.
[55] H. Han, J. Park, S.Y. Nam, et al., Nat. Commun. 10 (2019) 1471.
[56] J.H. Myung, D. Neagu, D.N. Miller, J.T. Irvine, Nature 537 (2016) 528–531.
[57] C. Ruan, K. Xie, Catal. Sci. Technol. 5 (2015) 1929–1940.
[58] G. Tsekouras, D. Neagu, J.T.S. Irvine, Energy Environ. Sci. 6 (2013) 256–266.
[59] S. Liu, Q. Liu, J.L. Luo, J. Mater. Chem. A 4 (2016) 17521–17528.
[60] X. Sun, Y. Ye, M. Zhou, et al., J. Mater. Chem. A (2022) 2327–2335.
[61] S. Ding, M. Li, W. Pang, et al., Electrochim. Acta 335 (2020) 135683.
[62] Y. Tian, Y. Liu, A. Naden, et al., J. Mater. Chem. A 8 (2020) 14895–14899.
[63] H. Lv, L. Lin, X. Zhang, et al., J. Mater. Chem. A 7 (2019) 11967–11975.
[64] H. Lv, L. Lin, X. Zhang, et al., Nat. Commun. 12 (2021) 1–11.
[65] J. Lu, C. Zhu, C. Pan, et al., Sci. Adv. 4 (2018) eaar5100.
[66] H. Lv, L. Lin, X. Zhang, et al., Adv. Mater. 32 (2020) 1906193.
[67] N. Han, R. Ren, M. Ma, et al., Chin. Chem. Lett. 33 (2022) 2658–2662.
[68] J. Sun, R. Ren, H. Yue, et al., Chin. Chem. Lett. 33 (2022) 107776.
[69] N.P. Brandon, S. Skinner, B.C. Steele, Annu. Rev. Mater. Res. 33 (2003) 183–213.
[70] J. Fleig, Annu. Rev. Mater. Res. 33 (2003) 361–382.
[71] K. Chen, N. Ai, Int. J. Hydrogen Energy 39 (2014) 10349–10358.
[72] S.B. Adler, Chem. Rev. 104 (2004) 4791–4844.
[73] M.A. Laguna-Bercero, A.R. Hanifi, H. Monzon, et al., J. Mater. Chem. A 2 (2014) 9764–9770.
[74] A. Chroneos, D. Parfitt, J.A. Kilner, R.W. Grimes, J. Mater. Chem. 20 (2010) 266–270.
[75] S. Streule, A. Podlesnyak, D. Sheptyakov, et al., Phys. Rev. B 73 (2006) 094203.
[76] A. Tarancón, D. Marrero-López, J. Peña-Martínez, et al., Solid State Ionics 179 (2008) 611–618.
[77] Q. Liu, C. Yang, X. Dong, F. Chen, Int. J. Hydrogen Energy 35 (2010) 10039–10044.
[78] Y. Tian, J. Li, Y. Liu, et al., Int. J. Hydrogen Energy 43 (2018) 12603–12609.
[79] Y. Tian, D. Yan, B. Chi, et al., ECS Trans. 78 (2017) 533.
[80] J. Laurencin, M. Hubert, D.F. Sanchez, et al., Electrochim. Acta 241 (2017) 459–476.
[81] Q. Lyu, N. Wang, Z. Li, et al., J. Power Sources 521 (2022) 230933.
[82] X. Zhang, S. Ohara, R. Maric, et al., J. Power Sources 83 (1999) 170–177.
[83] M.A. Laguna-Bercero, A.R. Hanifi, L. Menand, et al., Electrochim. Acta 268 (2018) 195–201.
[84] L. Mingyi, Y. Bo, X. Jingming, C. Jing, Int. J. Hydrogen Energy 35 (2010) 2670–2674.
[85] H. Fan, M. Keane, N. Li, et al., Int. J. Hydrogen Energy 39 (2014) 14071–14078.
[86] N. Li, L. Wang, M. Wang, et al., J. Power Sources 518 (2022) 230787.
[87] X. Wang, B. Yu, W. Zhang, et al., Int. J. Hydrogen Energy 37 (2012) 12833–12838.
[88] M.S. Khan, X. Xu, R. Knibbe, Z. Zhu, ACS Appl. Mater. Interfaces 10 (2018) 25295–25302.
[89] H. Xu, B. Chen, J. Irvine, M. Ni, Int. J. Hydrogen Energy 41 (2016) 21839–21849.
[90] Y. Wang, T. Liu, S. Fang, et al., J. Power Sources 277 (2015) 261–267.
[91] C. Zhu, S. Hou, X. Hu, et al., Nat. Commun. 10 (2019) 1173.
[92] Y. Song, L. Lin, W. Feng, et al., Angew. Chem. Int. Ed. 58 (2019) 16043–16046.
[93] L. Lei, Y. Wang, S. Fang, et al., Appl. Energy 173 (2016) 52–58.
[94] X. Zhang, L. Ye, H. Li, et al., ACS Catal. 10 (2020) 3505–3513.
[95] M. Li, B. Hua, L.C. Wang, et al., Nat. Catal. 4 (2021) 274–283.
[96] Z. Pan, C. Duan, T. Pritchard, et al., Appl. Catal. B 307 (2022) 121196.

[97] J.C.W. Mah, A. Muchtar, M.R. Somalu, M.J. Ghazali, Int. J. Hydrogen Energy 42 (2017) 9219–9229.
[98] E. Dogdibegovic, S. Ibanez, A. Wallace, et al., Int. J. Hydrogen Energy 47 (2022) 24279–24286.
[99] P. Piccardo, R. Spotorno, C. Geipel, Energies 15 (2022) 3458.
[100] K. Singh, T. Walia, Int. J. Energy Res. 45 (2021) 20559–20582.
[101] A. Hauch, J.R. Bowen, L.T. Kuhn, M. Mogensen, Electrochem. Solid St. 11 (2008) B38–B41.
[102] Y. Zheng, Q. Li, W. Guan, et al., Ceram. Int. 40 (2014) 5801–5809.
[103] Y. Zheng, Q. Li, T. Chen, et al., Int. J. Hydrogen Energy 40 (2015) 2460–2472.
[104] X. Zhang, J.E. O'Brien, R.C. O'Brien, et al., Int. J. Hydrogen Energy 38 (2013) 20–28.
[105] J. Mougin, A. Chatroux, K. Couturier, et al., Energy Procedia 29 (2012) 445–454.
[106] Q. Fang, L. Blum, N.H. Menzler, J. Electrochem. Soc. 162 (2015) F907–F912.
[107] M. Reytier, S. Di Iorio, A. Chatroux, et al., Int. J. Hydrogen Energy 40 (2015) 11370–11377.
[108] M. Riedel, M.P. Heddrich, A. Ansar, et al., J. Power Sources 475 (2020) 228682.
[109] R. Küngas, P. Blennow, T. Heiredal-Clausen, et al., ECS Trans. 91 (2019) 215–223.